Polymer 50 (2009) 2123–2132

Contents lists available at ScienceDirect

Polymer

journal homepage: www.elsevier.com/locate/polymer

Spatial statistics of carbon nanotube polymer composites

S. Pegel [a], P. Pötschke [a,*], T. Villmow [a], D. Stoyan [b], G. Heinrich [a]

[a] Leibniz-Institut für Polymerforschung Dresden e.V., Hohe Str. 6, 01069 Dresden, Germany
[b] TU-Bergakademie Freiberg, Institut für Stochastik, Prüferstraße 9, 09596 Freiberg, Germany

ARTICLE INFO

Article history:
Received 10 December 2008
Received in revised form
19 February 2009
Accepted 20 February 2009
Available online 26 February 2009

Keywords:
Carbon nanotube composites
Microstructure
Statistical geometry

ABSTRACT

Dispersion, distribution, and alignment of carbon nanotubes (CNT) in polycarbonate (PC) composites are quantified by means of statistical analysis of transmission electron microscopy (TEM) images. The analysed images originate from samples with 0.875 and 2 wt% CNT, processed by compression and injection moulding, respectively. The composites exhibit different microstructures with different electrical properties, depending on the processing parameters. By means of stereological approaches for projections of three dimensional fibre systems the CNT contents within the TEM samples are estimated. The tendency of CNT clustering as well as characteristic distances between the CNT and CNT clusters are quantified by evaluation of morphological functions. Furthermore, a correlation function is introduced to obtain a quantitative measure of CNT clustering within the isotropic compression moulded samples. For the injection moulded samples the correlation function is used to derive local orientation factors. The results underline that clustering of CNT can enhance and alignment of tubes can reduce electrical conductivity.

1. Introduction

During the last decade many researchers put efforts on the development of carbon nanotube polymer composites. Due to their extraordinary electrical properties, high mechanical strength and flexibility, in combination with large aspect ratios, CNT are a very promising type of filler [1,2]. The aim of transferring these unique properties to macroscopic scales has been realised by application of composite preparation techniques such as solution casting [3,4], in situ polymerisation [5,6], and melt processing [7–9]. In all cases, the key factor is control of CNT dispersion, distribution, arrangement, and orientation (CNT microstructure) within the host matrix.

One of the major problems in CNT composite research is to obtain a suitable dispersion and distribution of the filler. The individualisation of CNT from primary agglomerates is very difficult due to high van der Waals forces and physical entanglements. Very important are processing conditions and choice of base materials. An accurate measure of CNT dispersion and distribution is essential to find relationships between processing, structure, and properties of CNT composites. However, up to date only a few methods are reported and applied to obtain quantitative statements of CNT dispersion and distribution.

The analysis of optical micrographs is rarely performed and no standard has been established yet. The macro dispersion index as used for the characterisation of carbon black composites [10–12] can help to quantify optimal processing conditions as recently demonstrated for poly(lactic acid)/CNT composites [9]. Some evaluation methods also consider size distributions [13] and relative spatial positions of CNT agglomerates [14]. Alternatively, UV–vis and near infrared absorption measurements have been utilised to quantify the state of CNT dispersion [14]. However, relative positions of individual CNT as well as the structure of agglomerates or clusters on a submicron scale cannot be determined by these methods. Nevertheless, cluster formation of CNT at submicron scales has a large impact on the electrical conductivity [15]. In this article we applied techniques of image processing, stereology, and spatial statistics to TEM micrographs of earlier studies [15,16] to obtain objective measures of CNT dispersion and information about agglomerate structures.

CNT alignment is another important aspect of CNT microstructure. Previously, CNT alignment was measured by performing X-ray [17–20] or Raman [19,21–23] scattering experiments. However, these methods average the CNT orientation over large volumes, which can also be disadvantageous if a high spatial resolution is needed. Furthermore, these methods cannot be applied for samples with low filler contents, because of insufficient signal-to-noise ratios.

To obtain information about CNT alignment with high spatial resolution even at low filler contents the analysis of micrographs can be applied. Shaffer for instance, used the power spectrum to calculate local order parameters of different CNT films [24]. In the second part of this article we use a closely related correlation function to quantify local CNT alignment of injection moulded samples of a former study [16].

* Corresponding author. Tel.: +49 351 4658 395; fax: +49 351 4858 565.
E-mail address: poe@ipfdd.de (P. Pötschke).

0032-3861/$ – see front matter © 2009 Elsevier Ltd. All rights reserved.
doi:10.1016/j.polymer.2009.02.030

In this paper, methods of spatial statistics were applied to TEM images of polycarbonate filled with multiwalled carbon nanotubes by melt mixing and typical TEM images were analysed. Polycarbonate was selected as an example due to the availability of suitable TEM images, however, it can assumed that the described techniques can be applied to other CNT/polymer composites and some of the concepts can also be adapted to systems containing other nanoparticles.

2. Theoretical background

We applied spatial statistics and image processing techniques to extract microstructural characteristics of three-dimensional samples using planar TEM images. This is a fundamental part of stereology. Since the most readers are probably not familiar with this topic a brief introduction is given here (cf. [25–27] for further information).

TEM images of CNT composites are projections of three dimensional (3d) fibre systems onto a plane. An important first order characteristic of a 3d fibre system is the specific fibre length per volume unit J_V. If the fibre segments are randomly oriented J_V is related to the specific fibre length per area unit L_A of the projected fibre system by:

$$J_V = \frac{4L_A}{\pi t}, \tag{1}$$

where t denotes the thickness of the thin section. A counting procedure may be applied to estimate L_A (Ham [28]):

$$L_A = \frac{\pi N}{2L}, \tag{2}$$

where L denotes the total length of a set of test lines that is placed over the image and N is the number of intersections with the projected fibre system.

The investigation of so called second order characteristics of the CNT microstructure, i.e. to describe dispersion and distribution, of 3d samples by means of TEM images is a rather complicated issue. Clearly, the projection of the CNT microstructure on a plane involves a large loss of information. As a consequence, the estimation of 3d characteristics may be quite inaccurate since it requires the solution of ill-posed problems. Therefore, we restrict our considerations to the second order characteristics of the projected CNT microstructure. We assume that the dispersion and distribution of this planar pattern reflect in some way the situation in the three dimensional space, i.e. if the CNT appear clustered in a TEM image we assume the CNT to be clustered in the corresponding 3d space.

A given CNT microstructure or its projection on a plane can be mathematically treated as realisation of a random closed set (RCS). Based on grey valued raster graphics such as TEM images, the definition of the realised RCS is carried out by segmentation, in a two-phase system called binarisation. Binarisation sets all image pixels to either zero (white) or one (black). The RCS Ξ is than given by the union of black image pixels.

The second order characteristics of Ξ may be characterised by investigation of its so-called morphological functions $A_A(r)$ and $N_A(r)$ [26]. $A_A(r)$ is the area fraction and $N_A(r)$ is the specific Euler number[1] of Ξ dilated with a disc of radius r[2].

Fig. 1 illustrates some basic properties of the morphological functions. Two systems of bars Ξ_1 and Ξ_2 with different arrangements are shown. Both have the same area fraction p. The first system Ξ_1 (Fig. 1a) is characterised by clustered bars, where the distances between the nearest neighbours are comparatively short and larger empty domains between the clusters can be observed. The second system Ξ_2 (Fig. 1d) exhibits homogeneously distributed bars with larger distances between the nearest neighbours. Due to these differences the dilation of Ξ_1 and Ξ_2 has different effects. Fig. 1b and e show both sets dilated with $b(\boldsymbol{o},r_1)$. In case of the clustered bars formerly disjoined regions are connected, whereas the homogenously distributed bars remain disjoined. Consequently, different bar arrangements lead to different morphological functions. $A_A(r)$ of Ξ_1 exhibits a weaker convergence to one as compared to Ξ_2 (Fig. 1c) because large dilation radii are needed to fill the empty domains outside the clusters. On the other hand the smaller next neighbour distances inside the clusters decrease the specific Euler number already at small dilation radii (Fig. 1f). Assuming an observation window of unit area the specific Euler numbers of Ξ_1 and Ξ_2 dilated with $b(\boldsymbol{o},r_1)$ are 0 and 6 per unit area, respectively (Fig. 1b,e).

The morphological function $A_A(r)$ of a given Ξ obtained with a disc as structuring element, can be used to estimate the empirical spherical contact distribution function, $\widehat{H}_S(r)$ Eq. (3). $\widehat{H}_S(r)$ can be interpreted as the distribution function of the shortest distance of a random point $\boldsymbol{x}$ to Ξ, given that $\boldsymbol{x}$ is located outside Ξ [25].

$$\widehat{H}_S(r) = 1 - \frac{1 - A_A(r)}{1 - p} \tag{3}$$

The use of spherical contact distribution functions is advantageous, because some theoretical models are available to obtain characteristics of empirical data. In case that a RCS is represented as a planar pattern of line segments with a uniform random distribution (Poisson distribution) and orientation in plane, the spherical contact distribution function follows Eq. (4) (Boolean model). The mean length of segments is denoted by m_1. The intensity λ represents the number of segments per unit area.

$$H_S(r) = 1 - e^{-\lambda r(2m_1 + \pi r)} \tag{4}$$

A second possibility to characterise the dispersion of a realised RCS is the investigation of the covariance [25] or two point probability function [29]. The covariance $C(\boldsymbol{r})$ of a RCS Ξ is defined by the probability P that a randomly chosen point $\boldsymbol{x}$ and a second point located at $\boldsymbol{x}+\boldsymbol{r}$ both belong to Ξ Eq. (5).

$$C(\boldsymbol{r}) = P(\boldsymbol{x} \in \Xi, \boldsymbol{x} + \boldsymbol{r} \in \Xi) \tag{5}$$

In the planar case $C(\boldsymbol{r})$ can be interpreted as the area fraction of the intersection of Ξ with Ξ shifted by the vector $\boldsymbol{r}$, $A_A(\Xi \cap (\Xi + \boldsymbol{r}))$ (Fig. 2a,b). Following this procedure for all discrete vectors $\boldsymbol{r}$ in the range of the image size leads to an intensity map as shown in Fig. 2c. The intensity distribution strongly depends on the appearance of Ξ. In this example the anisotropic character is reflected by a strongly elliptical intensity distribution.[3] The regularity of distribution (distance between the bars in Fig. 2a) is described by the periodicity of intensity in x-direction (Fig. 2c and d).

As the covariance satisfies the properties $C(0) = p$ and $C(\infty) = p^2$, the covariance function can be derived by subtraction of p^2. The

[1] In the planar case the Euler number equals the number of outer boundary components minus the number of inner boundary components. N_A is the Euler number referenced to the area.

[2] The mathematical operation of dilation is also known as Minkowski-Addition and denoted by $\oplus$. A disc with radius r centred at the origin $\boldsymbol{o}$ is denoted by $b(\boldsymbol{o},r)$.

[3] Isotropic pattern exhibit a radial, angular independent intensity distribution, based on the image centre and thus: $\boldsymbol{r} \to r$ as well as $C(\boldsymbol{r}) = C(r)$ and $\kappa(\boldsymbol{r}) = \kappa(r)$.

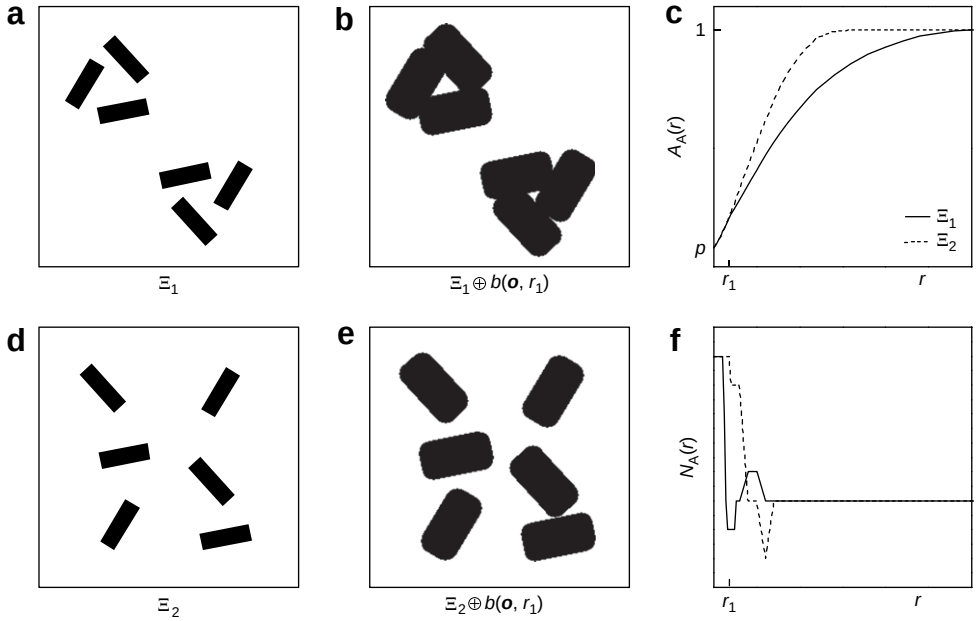

Fig. 1. (a, b) and (d, e) Effect of dilation to two RCS with the shape of six isolated bars, (c, f) corresponding morphological functions $A_A(r)$ and $N_A(r)$.

normalisation with $p(1-p)$ leads to the correlation function $\kappa(\boldsymbol{r})$ Eq. (6).

$$\kappa(\boldsymbol{r}) = \frac{C(\boldsymbol{r}) - p^2}{p(1-p)} \tag{6}$$

Practically, the covariance of a realisation of a RCS imaged on a raster graphic can be obtained by autocorrelation. For this purpose the most image processing programs use algorithms based on Fast Fourier Transformation (Wiener–Khinchin theorem).

3. Experimental techniques

3.1. Materials

3.1.1. Compression moulded polycarbonate containing 0.875 wt% MWNT [15]

A masterbatch with 15 wt% multiwalled carbon nanotubes (MWNT) (Hyperion Catalysis International, Inc., Cambridge, MA, USA) was diluted with polycarbonate PC Lexan 121 (GE Plastics, Europe) to obtain composites with 0.875 wt% MWNT. These MWNT are processed by chemical vapour deposition and exhibit a hollow curved structure. The dimensions are reported to be roughly 5 and 10 nm for the inner and outer diameters and the aspect ratios are between 100 and 1000 [30]. However, measurements by Pötschke et al. applying TEM resulted in a mean outer diameter of 12 nm [31], which seems to be more accurate. Therefore, this value has been used for the subsequent calculations. The density is assumed to be close to the value of 1.75 g/cm^3 reported by Shaffer [4]. With a density of 1.19 g/cm^3 for polycarbonate, the volume fraction of MWNT within this composite can be declared as 0.60 vol%. The composite was prepared by melt mixing the materials at 265 °C and 50 rpm for 15 min with a microcompounder (Daca Instruments, Goleta, CA, USA). The extruded strands, which exhibit a very homogenous MWNT dispersion, were compression moulded into plates. In dependence on the compression moulding conditions samples with different dielectrical properties were obtained.

The sample PC-CM1 was pressed at 250 °C with a pressing speed of 6 mm/min. Dielectrical measurements revealed no electrical percolation of the MWNT within this sample (conductivity below 10^{-16} S/cm at low frequencies). TEM images of thin sections with thicknesses of approx. 120 nm indicate the presence of only small agglomerates and many individualised MWNT. Fig. 3a shows one of three images investigated in this study.

The sample PC-CM2 was compression moulded at 300 °C with 0.5 mm/min. The dielectric measurements reveal a very pronounced plateau of the electrical conductivity at around 10^{-3} S/cm at low frequencies. TEM images of this plate show a rudimentary network structure with extended agglomerates. Fig. 3b shows one of three analysed images.

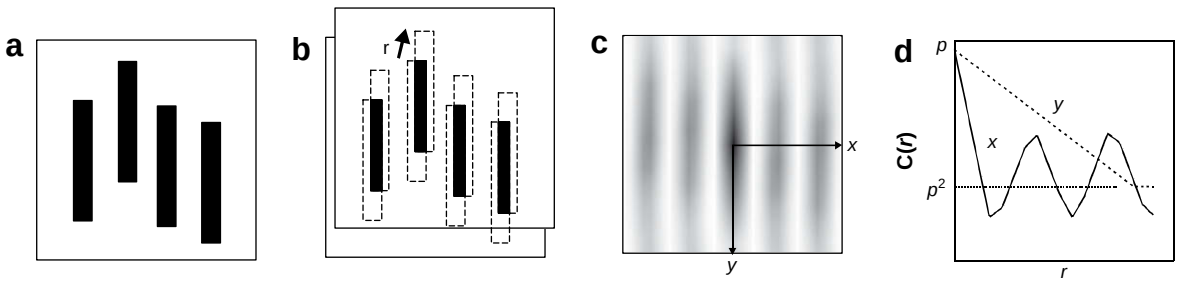

Fig. 2. (a–d) Example for a covariance analysis of a given RCS.

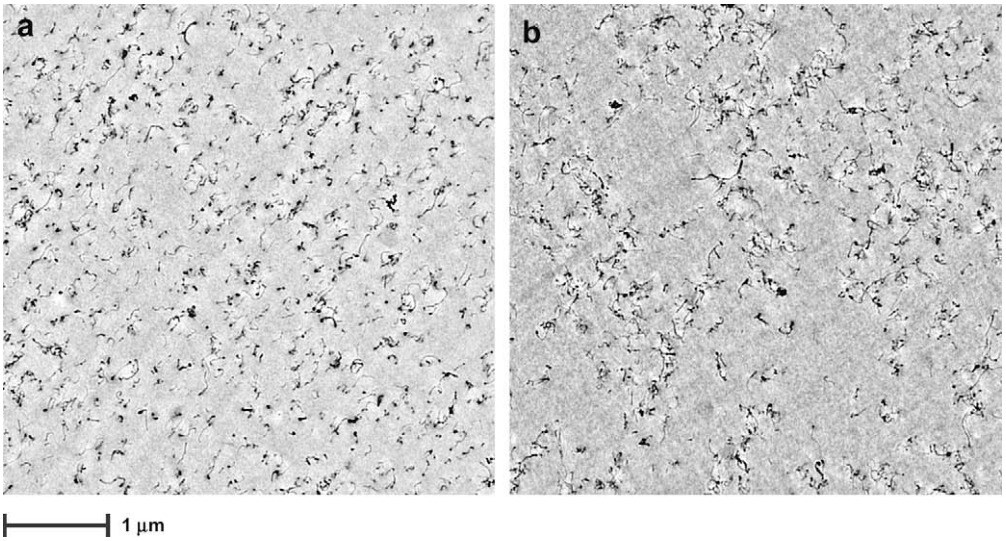

Fig. 3. TEM micrographs of polycarbonate with 0.875 wt% MWNT compression moulded at (a) PC-CM1: 250 °C with 6 mm/min (no electrical percolation) and (b) PC-CM2: 300 °C with 0.5 mm/min (σ_{DC} plateau above 10^{-4} S/cm). A Fourier band pass filter (2–50 pixels) was applied to reduce shading and to enhance the contrast between CNT and background.

3.1.2. Injection moulded polycarbonate containing 2 wt% MWNT [16]

Composites of polycarbonate with 2 wt% MWNT (1.37 vol%) were prepared by diluting the same masterbatch as used for the previous samples. The dilution process was carried out with PC Makrolon® 2600 (Bayer Material Science, Germany) on a ZE 25 extruder with two co-rotating screws (Berstorff, Germany) at a barrel temperature of 295 °C, a screw speed of 200 rpm, and a throughput of 10 kg/h. In the next step the granulated and properly dried material was injection moulded (Ergotech $100/_{420}$-310, Demag, Germany) into plates with $80 \times 80 \times 2$ mm^3 under varied conditions. To extract the injection moulding parameters with the strongest impact on the electrical conductivity an experimental design with two levels of four factors was evaluated. The studies pointed out that injection velocity and melt temperature highly influence the electrical conductivity. TEM investigations of two selected samples, in the following named PC-IM1 and PC-IM2, with distinct differences of electrical properties were performed (Table 1). Thin sections of approx. 150 nm were cut perpendicular to the surface and parallel to the flow direction (see [16] for further details). Several images were taken at different distances to the sample surface i.e. mould wall (Figs. 4 and 5).

The low electrical volume conductivity of PC-IM1 (approx. 10^{-13} S/cm) was referred to a distinct alignment of MWNT in the near of the sample surface (2 µm, Fig. 4a). At a sample depth of 43 µm the orientation is much less pronounced (Fig. 4b). Furthermore, the MWNT seem to be quite good dispersed and distributed.

The sample PC-IM2 exhibits a more clustered and less oriented MWNT arrangement (see Fig. 5a,b). This sample possesses a volume conductivity of 10^{-8} S/cm. Furthermore, it seems that the MWNT arrangement does not change very much with increasing distance to the mould wall.

Table 1
Injection moulding parameters and sample conductivities.

Sample	Injection velocity	Melt temperature	Holding pressure	Mold temperature	Mean volume conductivity
PC-IM1	150 mm/s	280 °C	40 bars	60 °C	10^{-13} S/cm
PC-IM2	10 mm/s	320 °C	40 bars	100 °C	10^{-8} S/cm

3.2. Image processing and structure analysis

The image processing was done with the Java based open source software ImageJ. The original TEM images were processed with a Fourier band pass filter (2–50 pixels) to reduce shading and to enhance the contrast between CNT and background (Figs. 3–5).

3.2.1. Binarisation

Binarisation is usually carried out by application of a threshold to the grey value of the image. However, practically it was not easy to obtain properly segmented images. If the threshold was set too low some background pixels have been converted to black. If the threshold was too high some MWNT have not been captured. Therefore, the following procedure was chosen: The threshold was set to a limit were only MWNT were captured. The image was binarised and the background pixels were set to be transparent. This image was superimposed to the original grey value image and printed out. MWNT which were not captured by the threshold have been blackened with a pen. The images were scanned, cropped, and resized to 1024×1024 pixels. Afterwards, an accurate threshold could be set to assign the pixels to the MWNT phase prior binarisation. Larger artefacts have been removed manually. Noise, viz. particles smaller than eight pixels, were removed by application of the particle size filter of the "Particles8_Plus" plug-in provided by Landini [32].

3.2.2. Estimation of the MWNT content in the TEM images

An instruction macro was programmed to superimpose a system of vertical and horizontal test lines with a regular distance of 10 pixels to the binary image. The instruction macro also counts the number of intersections with the projected CNT and L_A was estimated by means of Eq. (2). J_V was obtained by means of L_A and Eq. (1). The MWNT volume fraction was estimated with Eq. (7).

$$V_V = \frac{\pi d^2 J_V}{4} \tag{7}$$

3.2.3. Estimation of morphological functions

Another instruction macro was programmed to perform repeated dilations on the original binary image. Discs with different radii were used as structuring elements. For this purpose code

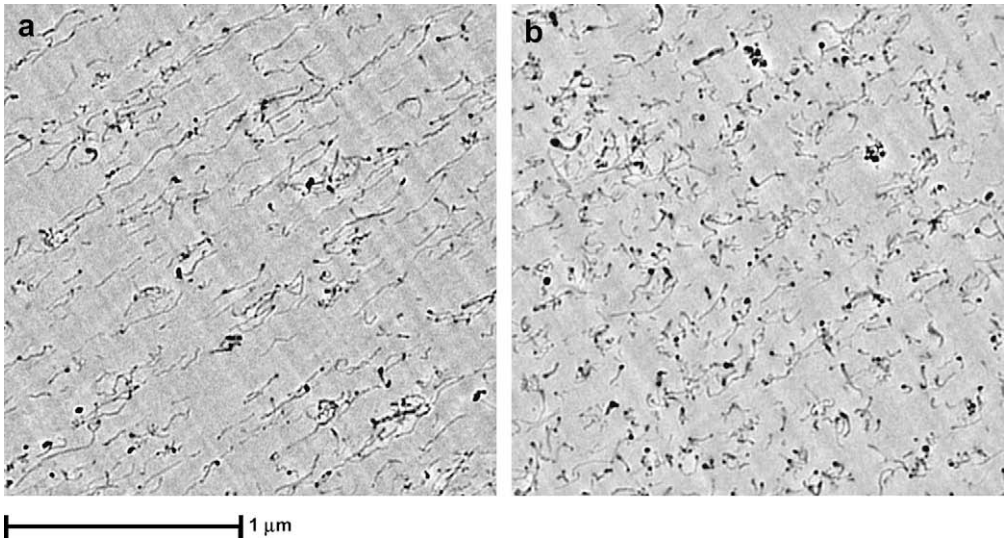

Fig. 4. Selection of TEM images of PC-IM1 at a depth of (a) 2 µm and (b) 43 µm to the sample surface. A Fourier band pass filter (2–50 pixels) was applied to reduce shading and to enhance the contrast between CNT and background.

published in [33] was used. The area of all particles[4] was obtained by means of the "Particles8_Plus" plug-in [32]. The area fraction of the dilated images was derived from the cumulative area of the particles. The Euler number was evaluated using code similar to the "hole counter" macro [34].

3.2.4. Investigation of the correlation function $\kappa(\boldsymbol{r})$

The FD Math algorithm implemented in ImageJ was used to get the autocorrelation of the binary images. The autocorrelation image was divided by $(255 \cdot 1024)^2$ to obtain the covariance.[5] The correlation function $\kappa(\boldsymbol{r})$ was obtained by application of Eq. (6).

The orientation analysis was carried out by means of a macro which processes the 2d correlation function (grey valued image) as follows: a squared selection (256 by 256 pixels) of the image centre was copied into a new image. The new image was resized to 1024 by 1024 pixels with interpolation of grey values. A selection has been created by application of a grey value threshold and an elliptical fit was performed. The mean direction of the ellipses major axis was determined (main CNT orientation). $\kappa(r)$ was evaluated along the major and lateral[6] axis.

4. Results and discussion

4.1. Dispersion, distribution, and agglomerate structure

A relatively simple method to obtain information about the CNT dispersion and distribution is the estimation of the CNT content observed in TEM images by means of Eq. (7). The data for the compression moulded samples are listed in Table 2. With 0.69 and 0.70 vol% for PC-CM1 and PC-CM2 the mean values are only slightly above the volume content which can be expected due to the composite formulation (0.6 vol%). Most probably the error results from an overestimation of the MWNT diameter reported in [31]. The knowledge of the accurate CNT diameter is essential for the correctness of the calculations due to the quadratic relation between d and V_V. Nevertheless, the results underline the good macroscopic dispersion since the expected volume content is reflected on a microscopic scale. For macroscopically badly dispersed samples the amount of CNT within the TEM images would be much higher or lower in dependence whether the thin sections contain agglomerates or not. Furthermore, the CNT seem to be macroscopically well distributed as samples taken at different positions contain more or less the same amount. In other words, a bad dispersion and distribution would result in a large variance of the CNT content. The number density of CNT can be estimated by means of J_V and values between 55 and 69 tubes per μm^3 are obtained, assuming a mean CNT length of 1 µm.

Additionally, the estimation of CNT content within TEM images enables the possibility to investigate migrations of CNT at high spatial resolution. Fig. 6 shows the volume content plotted against the distance d to the mould wall for the injection moulded samples. It seems like there is no distinct tendency for CNT migration. However, it has to be considered that some values are overestimated due to alignment of the CNT near the mould wall (Section 4.2). The CNT are displayed in full length and J_V rather equals L_A/t, if the CNT are oriented in a plane parallel to the projection plane (i.e. TEM image). With Eq. (1) it comes clear that the CNT contents near the mould wall are overestimated by factors between $4/\pi$ and 1 depending on the degree of alignment. And thus the curves in Fig. 6 would exhibit a steeper slope. The error caused by an inaccurate estimation of the CNT diameter would only lead to a y-directional shift of the curves but would not change their shapes. The values of the CNT content are in the range of 1.55–2.18 vol% and thus overestimated compared to the expected value of 1.37 vol%. Nevertheless, the results clarify that a migration of CNT is not responsible for the differences of the electrical properties between the samples PC-IM1 and PC-IM2.

The appearance of CNT microstructure observed in the TEM images reveals that the different electrical properties are clearly related to differences of the relative positions and orientation of individual CNT. For the investigation of CNT clustering, the morphological functions $A_A(r)$ and $N_A(r)$ of the corresponding realisations of the RCS have been analysed. In Figs. 7 and 8 the results of the compression moulded samples are shown. Three different TEM images were considered for each sample. In both

[4] The area inside the polygon defined by the perimeter of the particle.

[5] In ImageJ the black pixels are assigned with a value of 255. The image size was 1024^2 pixels.

[6] Perpendicular to the major axis.

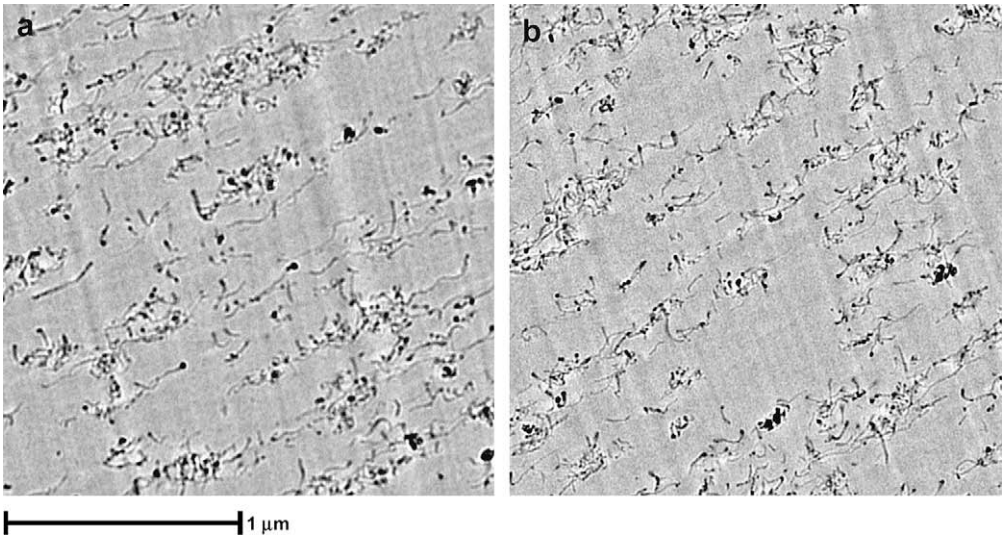

Fig. 5. Selection of TEM images of PC-IM2 at a depth of (a) 3 µm and (b) 27 µm to the sample surface. A Fourier band pass filter (2–50 pixels) was applied to reduce shading and to enhance the contrast between CNT and background.

diagrams two different sets of curves can be clearly distinguished due to the distinct differences of the CNT microstructure.

Since both materials contain approximately the same CNT content, the CNT clustering in PC-CM2 results in larger empty areas between the clusters. The more homogeneous distribution of the CNT in PC-CM1 is therefore well characterised by a more pronounced convergence of $A_A(r)$ to one as compared to PC-CM2 (Fig. 7).

Within the binarised TEM images the CNT clusters are represented as network like structures and clusters of overlapping curve segments. Thus, the corresponding realisations of the RCS of PC-CM2 are characterised by comparatively small specific Euler numbers (6–13 μm^{-2}). The dilation with small radii leads to closure of gaps between neighboured formerly disjoined regions, which results in a reduced number of disjoined regions and the formation of additional holes. Therefore, the function $N_A(r)$ decreases in this interval. With further increasing dilation radii more disjoined regions get connected and existing holes are completely closed. This causes a characteristic pronounced minimum of $N_A(r)$ for PC-CM2. This minimum is located at a dilation radius, which corresponds to the mean radius of the holes or gaps and thus represents the mean distance between the CNT within the clusters. It is approximately 10 nm. Furthermore, the curves show a local maximum above zero indicating the isolation of the clusters. If the clusters would be connected to a continuous network, only negative Euler numbers would be observed. The subsequent convergence to zero is related to the distance between the CNT clusters (i.e. the size of the empty areas).

In contrast to sample PC-CM2 in PC-CM1 the majority of the CNT is individualised. Accordingly the specific Euler numbers are comparatively large (26–32 μm^{-2}). Due to the more homogeneous distribution of the individual CNT, both, the distance distribution as well as the corresponding minimum of $N_A(r)$, are shifted to higher values. The characteristic distances are in the range between 70 and 120 nm for PC-CM1. Since no clustering occurs $N_A(r)$ converges directly to zero after the minimum.

We could show that the morphological functions are a meaningful tool to investigate the expansion of empty areas between individual CNT and CNT clusters. $A_A(r)$ is suitable to characterise the degree of clustering, i.e. cluster size due to the presence of larger empty areas. $N_A(r)$ is suitable to identify characteristic distances between individual CNT. However, the size of the empty areas or the space between neighbouring CNT also depends on the intensity λ (number of represented CNT per unit area). With increasing λ more CNT are spatially concentrated and the gaps between neighbouring CNT decrease as well. Correspondingly, the morphological functions depend on λ. To obtain a comparable measure for the distribution or dispersion at different intensities, the TEM images have to be transformed in a manner that distances between the centres of area of the imaged CNT are scaled by remaining their size, shape and orientation. As TEM micrographs are represented as raster graphics and a reconstruction with vector data as demonstrated for carbon blacks and silica by Tscheschel [35] remains a challenge due to the systems complexity and an exact adjustment is not possible at this state of the work.

However, assuming an even thickness of the thin sections, uniform random orientation and equal mean length m_1 of CNT, the images can be scaled to obtain comparable values of λ. The intensity within the observation window can be estimated with:

$$\lambda \approx \frac{L_A}{m_1} \tag{8}$$

If the length scale of a raster graphic is changed by a factor c, the area of the observation window scales with c^2. Since the number of imaged CNT remains constant, the scaled intensity λ^* is given by:

$$\lambda^* = \frac{\lambda}{c^2}. \tag{9}$$

To obtain an equal intensity the length scales have to be multiplied with a factor of $c = L_A^{0.5}$. However, the unification of intensity by scaling a raster graphic leads to different mean lengths and widths of the imaged CNT. Nevertheless, the resulting inaccuracy regarding

Table 2
Estimated values of specific fibre length J_V and volume fraction V_V of CNT in TEM images of compression moulded samples.

Material		J_V [μm^{-2}]	V_V [vol%]
PC-CM1	Image 1 (Fig. 3a)	68.5	0.78
	Image 2 (not shown)	58.7	0.66
	Image 3 (not shown)	55.9	0.63
PC-CM2	Image 1 (Fig. 3b)	66.4	0.75
	Image 2 (not shown)	54.7	0.62
	Image 3 (not shown)	65.2	0.74

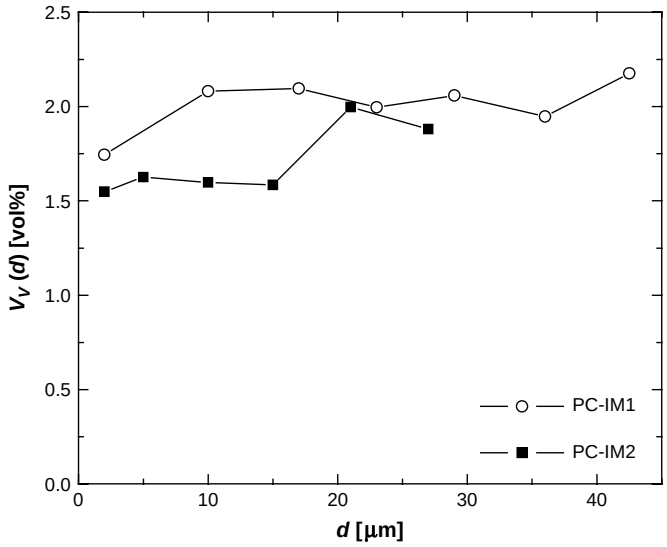

Fig. 6. CNT distribution of the injection moulded samples perpendicular to the mould wall.

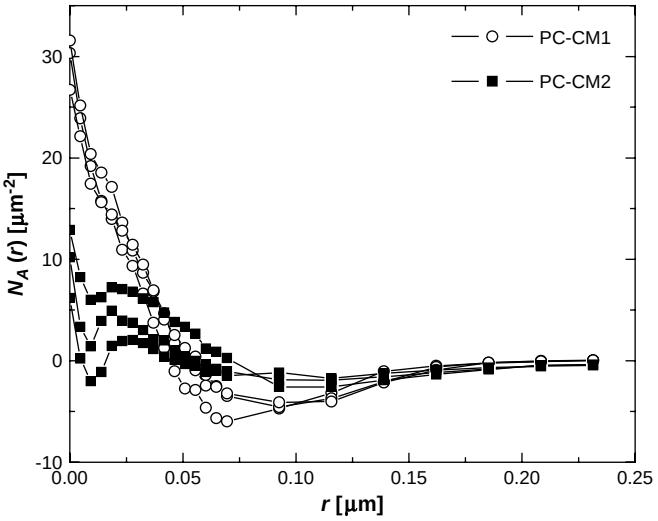

Fig. 8. Morphological function $N_A(r)$ of binarised TEM images of the compression moulded samples.

comparability of $A_A(r)$ is comparatively small especially if the differences of CNT content are not too high since the intensity scales quadratically and its impact is much higher in contrast to the mean length. This can be explained considering the spherical contact distribution function of the Boolean model for even line segments [25], which is closely related to $A_A(r)$ of the corresponding RCS. The intensity weights the quadratic term of Eq. (4).

Fig. 9 shows the empirical spherical contact distribution functions of the compression moulded samples. The dilation radii have been scaled to even intensity [$r^* = r(\lambda^* m_1)^{-0.5} L_A^{0.5}$ whereby$(\lambda^* m_1)^{-0.5}$ was set to 1 µm$^{-0.5}$]. The empirical contact distribution functions of PC-CM1 of all observation windows are almost equal. This indicates an even state of CNT distribution. Sample PC-CM2 is characterised by a bigger variance of the cluster size as indicated by larger differences of the curve shapes especially at high dilation radii. Again a slow convergence to one highlights the existence of CNT clusters and accordingly larger CNT-free areas.

For both samples the average of the three curves was calculated and a least square fit of Eq. (4) (Boolean fibre mode) performed. As shown in Fig. 7 the empirical data can be described quite well with this equation. Of course, the parameters λ^* and m_1^* obtained for scaled data have to be interpreted in a different manner since the preconditions of straight line segments and uniform random distribution are not satisfied. The fit parameters of both compression moulded samples are presented in Table 3. PC-CM1 exhibits a relatively large intensity in combination with a small mean length as compared to PC-CM2.

Beside the fit parameters we can use the area between the curves and the horizontal line at $H_S(r^*) = 1$ as a measure of CNT clustering tendency (Fig. 9). In the following this quantity will be denoted by S^*. The smaller the area the lesser the CNT tend to form clusters. The calculation can be carried out by means of the fit parameters and analytical integration of Eq. (4) or numerical integration of the empirical data. Due to non-dimensionality of $H_S(r^*)$ the integrals yield values with length units which are related to the size of the gaps between individual CNT or CNT clusters (of the scaled data). Values of S^* of approximately 0.12 and 0.16 µm have been determined for PC-CM1 and PC-CM2 by means of the fit parameters and analytical integration. In accordance with the

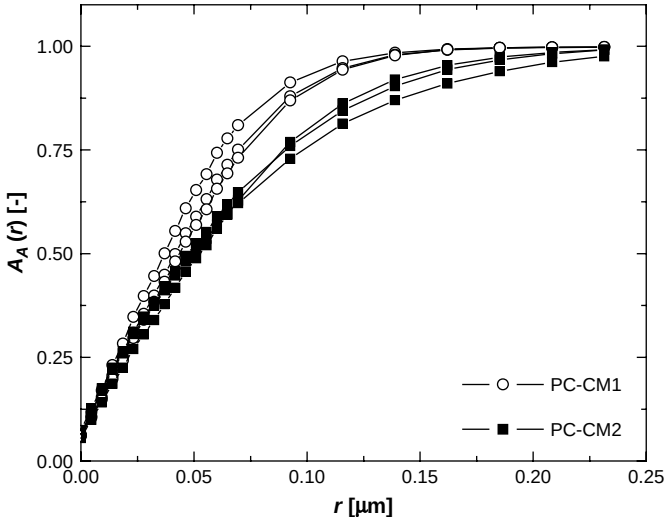

Fig. 7. Morphological function $A_A(r)$ of binarised TEM images of the compression moulded samples.

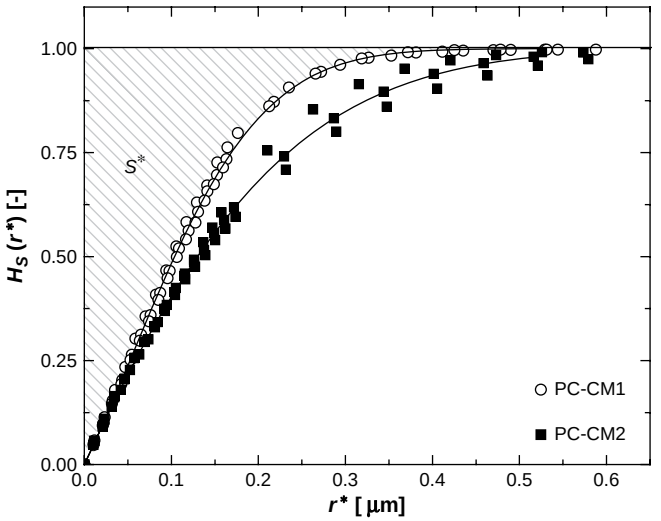

Fig. 9. Empirical spherical contact distribution functions of PC-CM1 and PC-CM2 as well as the corresponding least square fit of the Boolean model for even line segments.

Table 3
Fit parameter of the spherical contact distribution function of the Boolean model.

Sample	λ^* [μm^{-2}]	m_1^* [μm]
PC-CM1	7.42	0.29
PC-CM2	1.81	1.27

resistivity values the data show that formation of CNT clusters enhances conductivity. However, it is easy to imagine that the cluster structure also has a big impact on the network formation. To obtain electrical conductivity at low CNT contents, the CNT should be arranged in clusters which cover large volumes with low CNT numbers. Thus the corresponding RCS should be characterised by low Euler numbers combined with large holes (i.e. CNT-free areas) and thus a slow convergence of $A_A(r)$ and $H_S(r)$ to one.

TEM images of the injection moulded samples were analysed following the same procedure. The obtained values for S^* are plotted against the distance to the mould wall (Fig. 10). It can be noticed that all data points of PC-IM2 are located well above the data points of PC-IM1. This indicates a comparatively pronounced clustering of CNT in PC-IM2. Furthermore, PC-IM1 is characterised by homogeneous CNT distribution as compared to PC-IM2 exhibiting large variances. As demonstrated for compression moulded samples, the formation of electrically conductive networks requires clustering of CNT. However, a direct comparison between the compression and injection moulded samples is difficult due to the difference of CNT content as well as the different thin section thicknesses.

The evaluation of $N_A(r)$ revealed characteristic distances between 6 and 8 nm for CNT within the clusters of PC-IM2 (Fig. 11b). Furthermore, the clusters seem to be part of a network like structure since all curves converge towards zero without passing a pronounced local maximum. PC-IM1 exhibits some small clusters that result in a slight pronounced first local minimum or shoulder within the same range (6–8 nm, Fig. 11b). However, in contrast to PC-IM2 the curves of PC-IM1 exhibit a clear local minimum between 27 and 41 nm. Furthermore, no correlation between the distance to mould wall and location of the minima could be found.

Beside the morphological functions and the spherical contact distribution function the CNT microstructure can be analysed by means of the covariance or the closely related correlation function $\kappa(r)$. The use of the latter has the advantage that the data are

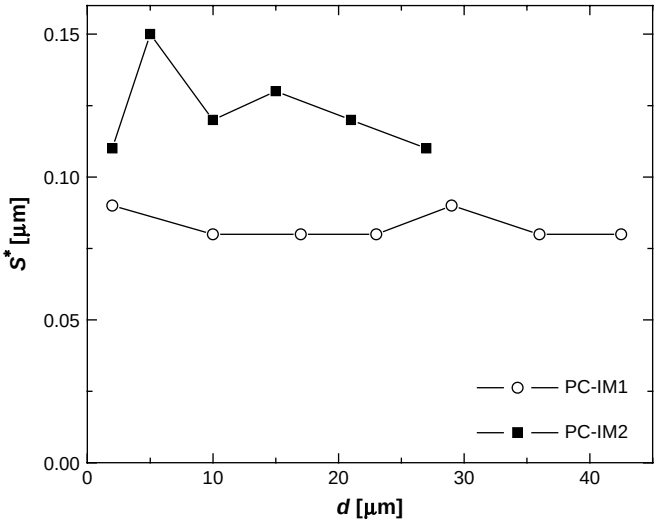

Fig. 10. The parameter S^* versus distance to the mould wall of the injection moulded samples PC-IM1 and PC-IM2.

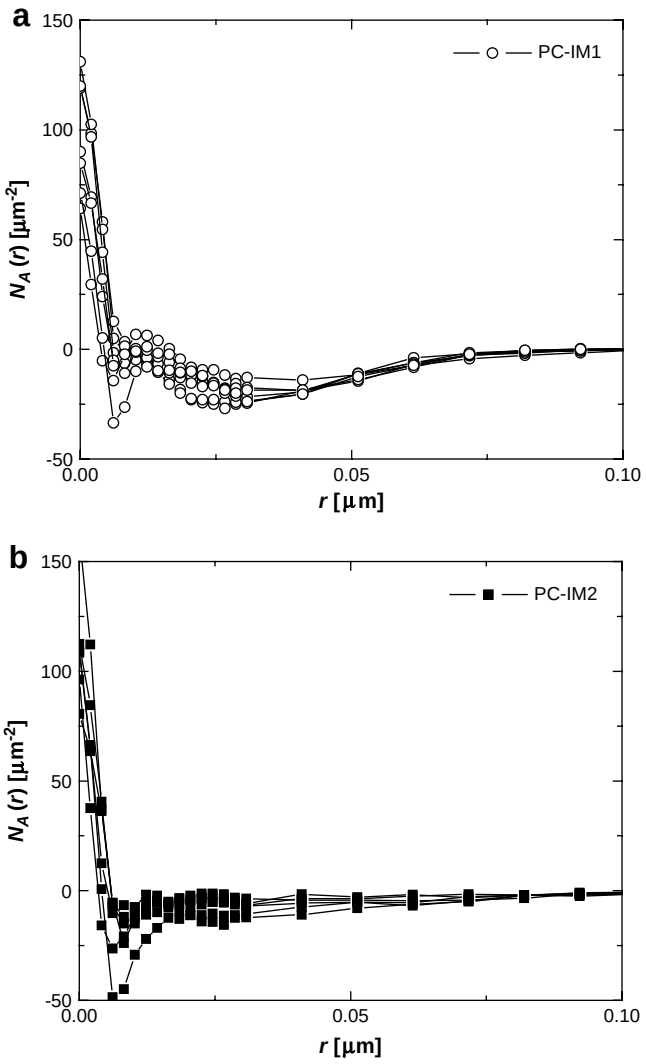

Fig. 11. Morphological function $N_A(r)$ of the binarised TEM images of the injection moulded samples (a) PC-IM1 and (b) PC-IM2.

normalized and thus small differences of filler content are equalised. Fig. 12 shows the corresponding correlation functions of the compression moulded samples. The homogeneous distribution of CNT in PC-CM1 is characterised by a fast convergence to zero of $\kappa(r)$ for all three images. In contrast, $\kappa(r)$ of PC-CM2 exhibits a much smaller convergence to zero. The convergence rate is obviously related to the CNT cluster size. With increasing cluster size the convergence rate decreases. As a measure of mean cluster size (and thus the tendency of CNT to form clusters), the area below the curves can be used. By numerical integration values in the range of 0.014–0.016 µm have been obtained for PC-CM1, whereas values between 0.019 and 0.028 µm where calculated for PC-CM2.

At this point it is worth to mention that the correlation functions theoretically also can be obtained by scattering experiments as well. Thus, for instance ultra small angle X-ray or light scattering experiments can be used to gain information about the dispersion or distribution in a larger sample volume.

4.2. Orientation of CNT

For anisotropic CNT microstructures the correlation function exhibits a comparatively easy way to determine filler alignment, even for raster graphics. As demonstrated in Section 2 anisotropic

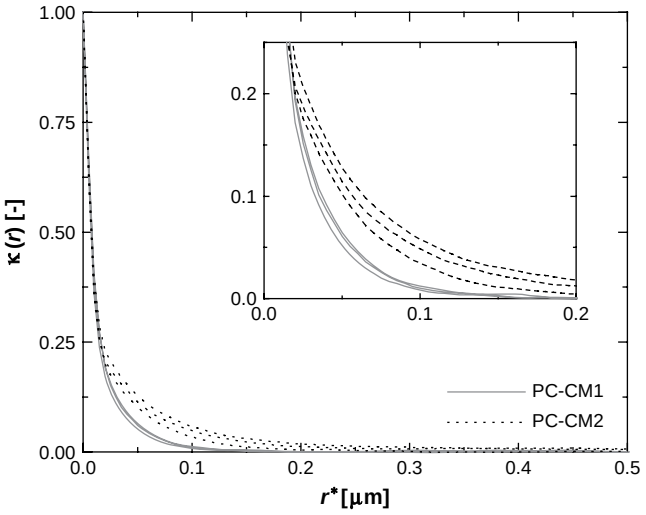

Fig. 12. Correlation functions of the compression moulded samples.

structures are characterised by differences of the covariance or its normalized form, the correlation function $\kappa(r)$, in different spatial directions. Fig. 13a and b show $\kappa(r)$ of the injection moulded sample PC-IM1 at 2 and 43 µm distance to the mould wall, where $\kappa(r)$ of the main direction of CNT alignment is denoted by the dashed graph. If existent, the main direction of CNT alignment is given by the major axis of the elliptical intensity distribution (Fig. 2). With increasing degree of alignment the correlation functions along the major and lateral axes are characterised by increasing differences in the convergence rate against zero. Thus PC-IM1 exhibits a comparatively strong CNT alignment close to the mould wall. At a distance of 43 µm to the mould wall almost no alignment can be detected since both correlation functions lay almost upon each other.

Furthermore, Fig. 13a shows two local extreme points of the correlation function in the direction perpendicular to the main CNT orientation. The intersection between the extrapolation of the linear part at the beginning of the correlation function and the horizontal line going through the minimum yields the mean CNT diameter. Here, a value of 9.2 nm was obtained, which is smaller than the reported 12 nm [31]. This can be explained with the rough discretisation (the images of this study where taken with a resolution of 2 nm per pixel).

Due to the comparatively regular distances between the CNT in lateral direction a local maximum of the corresponding correlation function can be observed. The maximum yields to a mean CNT distance of approx. 23 nm in PC-IM1 at 2 µm distance to the mould wall.

To obtain a measure for the alignment it is meaningful to consider only small correlation distances (in the range between the CNT diameter and the lateral spacing). Following this approach, correlations between different CNT remain unconsidered. According to Eq. (10) an orientation factor $O(x)$ can be defined by means of the ratio of the correlation functions at a distance x. Fig. 14 presents the orientation factors versus the distance d to the mould wall $O(16\text{ nm}, d)$ for both injection moulded samples. It can be seen, that the CNT of PC-IM1 are much stronger aligned as compared to PC-IM2, especially near the mould wall. The orientation decreases with increasing distance for both samples. Furthermore, it seems like there is a linear relationship between CNT orientation and distance to the mould wall up to 30 µm for both samples.

$$O(x) = 1 - \frac{\kappa_l(x)}{\kappa_m(x)} \tag{10}$$

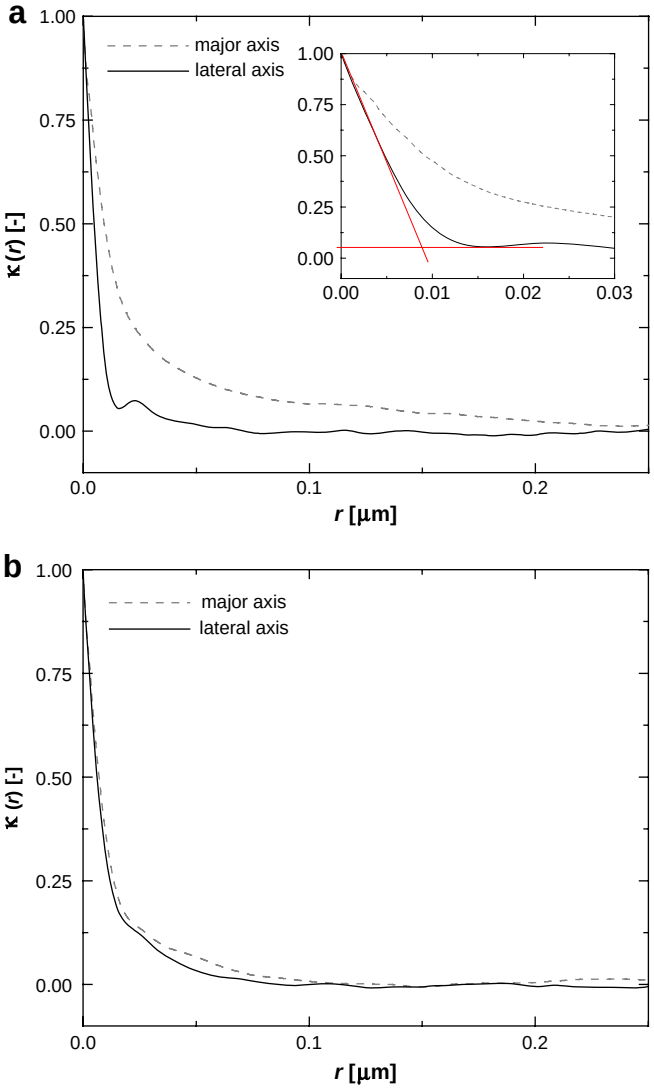

Fig. 13. Correlation functions of the injection moulded sample PC-IM1 at a distance of (a) 2 µm (Fig. 4a) and (b) 43 µm (Fig. 4b) to the mould wall.

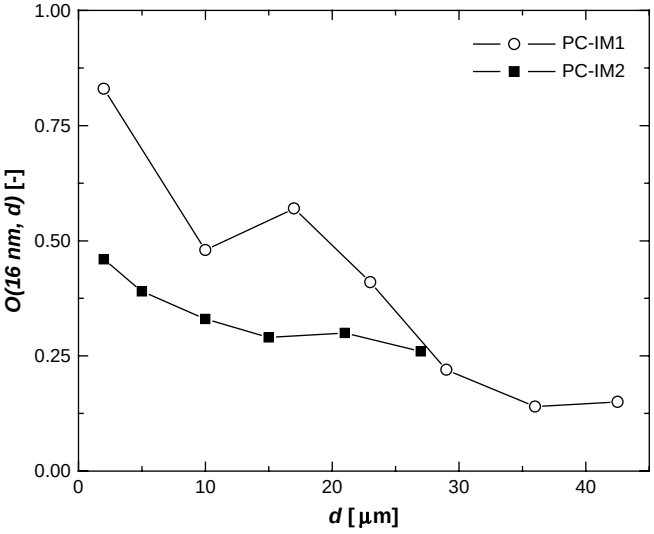

Fig. 14. Orientation factor versus distance to the mould wall of the injection moulded samples.

5. Summary and conclusions

Different morphological aspects of compression and injection moulded polycarbonate samples containing 0.875 and 2 wt% MWNT have been quantitatively analysed using TEM images. In each case two samples processed under different conditions leading to different typical microstructures have been investigated.

A stereological approach for isotropic fibre processes has been used to estimate local contents of disentangled CNT. For each compression moulded sample three TEM images from random locations have been evaluated. The CNT contents show only little variations and are close to the composite formulation. Thus, both compression moulded samples exhibit a good macroscopic dispersion and distribution. In case of the injection moulded samples the CNT content has been evaluated with increasing distance to the mould wall. No significant migration or depletion has been found.

The morphological functions $A_A(r)$ and $N_A(r)$ and the spherical contact distribution function $H_S(r)$ have been employed to the TEM images to access quantitative information about spatial relationships between individual CNT. In general, at the same CNT content the functions $A_A(r)$ and $H_S(r)$ of morphologies with clustered CNT are characterised by a stronger convergence to one as compared to those with Poisson distributed or repulsive CNT. As a measure for the tendency of CNT clustering the area S^* between $H_S(r^*)$ and $H_S(r^*) = 1$ has been used. To adjust the CNT content the scale has been normalized by means of the specific fibre length L_A. However, this can be done only for small differences since the scaling goes along with a change of the dimensions of the imaged CNT. For the compression as well as the injection moulded samples it has been found that the electrical conductivity is related to S^*. The samples with the higher conductivity exhibit the higher value of S^*.

Furthermore, a correlation function $\kappa(r)$ (derived from the covariance) has been used to investigate the CNT clustering within the compression moulded samples. The sample with pronounced CNT clustering exhibits the slower convergence of $\kappa(r)$ to one and thus a larger area below the curve. For the injection moulded samples $\kappa(r)$ has been used to obtain an orientation factor. The orientation factor has been evaluated as a function of the distance to the mould wall. The sample with the lowest conductivity exhibits strong CNT alignment in the near of the mould wall. At a distance of approximately 30 μm no differences of the CNT orientation have been found.

In this paper it has been demonstrated that different morphological characteristics of CNT polymer composites can be derived from TEM images by application of spatial statistics. The first order parameter CNT content can be obtained by a stereological approach for fibre processes. The second order parameters CNT dispersion, distribution, and alignment can be accessed with morphological functions and a correlation function. In principle, these concepts can also be applied to other microscopical methods, e.g. scanning electron microscopy or atomic force microscopy as well as to other nanocomposites if the corresponding images can be segmented properly. In addition, the techniques shown can be easily implemented using digital image processing and following calculations, thus, providing a relatively simple tool to quantify the microstructure.

With this adequate morphological characterisation it is now possible to interpret physical properties of CNT polymer composites more clearly. Of course, correlations between processing and structure, in particular the dispersion, can be drawn as well.

References

[1] Baughman RH, Zakhidov AA, de Heer WA. Science 2002;297(5582):787–92.
[2] Dresselhaus MS, Dresselhaus G, Avouris P. Carbon nanotubes: synthesis, structure, properties, and applications. Berlin; New York: Springer; 2001.
[3] Safadi B, Andrews R, Grulke EA. Journal of Applied Polymer Science 2002;84(14):2660–9.
[4] Shaffer MSP, Windle AH. Advanced Materials 1999;11(11):937–41.
[5] Broza G, Kwiatkowska M, Roslaniec Z, Schulte K. Polymer 2005;46(16): 5860–7.
[6] Sandler J, Shaffer MSP, Prasse T, Bauhofer W, Schulte K, Windle AH. Polymer 1999;40(21):5967–71.
[7] Breuer O, Sundararaj U. Polymer Composites 2004;25(6):630–45.
[8] Pötschke P, Fornes TD, Paul DR. Polymer 2002;43(11):3247–55.
[9] Villmow T, Pötschke P, Pegel S, Häussler L, Kretzschmar B. Polymer 2008;49(16):3500–9.
[10] Le HH, Tiwari M, Ilisch S, Radusch HJ. KGK. Kautschuk, Gummi, Kunststoffe 2005;58(11):575–80.
[11] ASTM D 2663 standard test methods for carbon black—dispersion in rubber; 2008.
[12] ISO, editor. ISO 18553: Method for the assessment of the degree of pigment or carbon black dispersion in polyolefin pipes, fittings and compounds; 2002.
[13] Li J, Ma PC, Chow WS, To CK, Tang BZ, Kim JK. Advanced Functional Materials 2007;17(16):3207–15.
[14] Kashiwagi T, Fagan J, Douglas JF, Yamamoto K, Heckert AN, Leigh SD, et al. Polymer 2007;48(16):4855–66.
[15] Pegel S, Pötschke P, Petzold G, Alig I, Dudkin SM, Lellinger D. Polymer 2008;49(4):974–84.
[16] Villmow T, Pegel S, Pötschke P, Wagenknecht U. Composites Science and Technology 2008;68(3–4):777–89.
[17] Sandler JKW, Pegel S, Cadek M, Gojny F, vanEs M, Lohmar J, et al. Polymer 2004;45(6):2001–15.
[18] Du F, Fischer JE, Winey KI. Physical Review B (Condensed Matter and Materials Physics) 2005;72(12):121404, 1–4. Available at: <http://prola.aps.org/abstract/PRB/v72/i12/e121404>.
[19] Fischer JE, Zhou W, Vavro J, Llaguno MC, Guthy C, Haggenmueller R, et al. Journal of Applied Physics 2003;93:2157.
[20] Jin L, Bower C, Zhou O. Applied Physics Letters 1998;73:1197.
[21] Wood JR, Zhao Q, Wagner HD. Composites Part A Applied Science and Manufacturing 2001;32(3–4):391–9.
[22] Pötschke P, Brünig H, Janke A, Fischer D, Jehnichen D. Polymer 2005; 46(23):10355–63.
[23] Bhattacharyya AR, Sreekumar TV, Liu T, Kumar S, Ericson LM, Hauge RH, et al. Polymer 2003;44(8):2373–7.
[24] Shaffer MSP, Fan X, Windle AH. Carbon 1998;36(11):1603–12.
[25] Stoyan D, Kendall WS, Mecke J. Stochastic geometry and its applications. John Wiley & Sons; 1995.
[26] Mecke KR. Additivity, convexity, and beyond: applications of Minkowski functionals in statistical physics. In: Mecke KR, Stoyan D, editors. Statistical physics and spatial statistics. The art of analyzing and modeling spatial structures and pattern formation. Berlin, Heidelberg: Springer-Verlag; 2000. p. 111–84.
[27] Ohser J. Statistical analysis of microstructures in materials science. New York: John Wiley; 2000.
[28] Ham RK. Philosophical Magazine 1961;6(69):1183–4.
[29] Torquato S. Random heterogeneous materials: microstructure and macroscopic properties. Springer; 2006.
[30] Ferguson DW, Bryant EWS, Fowler HC. ESD thermoplastic product offers advantages for demanding electronic applications. ANTEC 1998:1219–22.
[31] Pötschke P, Bhattacharyya AR, Janke A. European Polymer Journal 2004;40(1): 137–48.
[32] Landini G. Particles8_plus; 2007.
[33] Burger W, Burge MJ. Digital image processing: an algorithmic introduction using Java. New York: Springer-Verlag; 2008.
[34] Landini G. Hole counter; 2006.
[35] Tscheschel A. Räumliche Statistik zur Charakterisierung gefüllter Elastomere. Fakultät für Mathematik und Informatik, vol. PhD thesis. Freiberg: Technische Universität Bergakademie Freiberg; 2005.